Available online at www.sciencedirect.com
ScienceDirect
International Journal of Heat and Mass Transfer 51 (2008) 4841–4849
International Journal of HEAT and MASS TRANSFER
www.elsevier.com/locate/ijhmt

On the eruptive boiling in silicon-based microchannels

P.C. Lee, Chin Pan *

Department of Engineering and System Science, National Tsing Hua University, Hsinchu 30043, Taiwan

Received 21 June 2007; received in revised form 1 February 2008
Available online 16 April 2008

Abstract

This study investigates experimentally eruptive boiling in a silicon-based rectangular microchannel with a hydraulic diameter of 33.7 μm, a width of 99.8 μm and a depth-to-width ratio of 0.203. The microchannel is made of SOI wafer and prepared using bulk micro-machining and anodic bonding. The surface roughness for both the bottom and the side walls was measured using an atomic force microscope. The evolution of the eruptive boiling of water in the smooth microchannel was clearly observed using an ultra high-speed video camera (up to 50,000 frames/s) at mass fluxes of 417 and 625 kg/m^2 s and a heat flux from 14.9 to 372 kW/m^2. It is confirmed that eruptive boiling is a form of rapid bubble nucleation after which the bubble merges with a slug bubble downstream in a short distance or evolve to a slug bubble. The bubble frequency in all of the cases studied is provided. Eruptive boiling may be predicted classically with nano-sized cavities that are consistent with the measured surface roughness.

Keywords: Eruptive nucleate boiling; Microchannel

1. Introduction

As circuit density and operating speed increase, microprocessor heat fluxes may exceed 200 W/cm^2 by the end of the decade [1]. Highly efficient electronic cooling technologies are, therefore, very much in demand and various such technologies have been developed. Mudawar [2] reviewed different heat transfer techniques that are applied in electronic cooling, pool boiling, detachable heat sinks, channel flow boiling, microchannel and minichannel heat sinks, jet impingement and sprays. Microchannel heat sinks have been demonstrated to be high-performance cooling devices. "Eruptive boiling" in microchannels has been identified, such as by Zhang et al. [3], Jeong et al. [4] and Jiang et al. [5]. Eruptive boiling has been described as "boiling that occurs with no detectable bubble nucleation period" [3] and an event in which "two-phase flow appears as a single-phase liquid and a two-phase mist, separated by a fast oscillating interface in the longitudinal direction" [3]. Jeong et al. [4], citing the experimental observations of Jiang et al. [5], characterized eruptive boiling as a "change of the flow pattern from highly superheated liquid flow to annular mist flow by rapid bubble growth and quick filling of the channel cross section". However, they did not experimentally substantiate their statement. Hetsroni et al. [6] reported a phenomenon named "explosive boiling". They recorded a rapidly receding liquid–vapor meniscus with a rate of 1000 frames/s. Hardt et al. [7] reported similar eruptive meniscus evaporation with a rate of 5000 frames/s. In their study, no bubble nucleation was detected. Moreover, they commented that "the question whether or not there is a boiling mechanism in microchannels not being initiated by bubble nucleation seems to be not yet resolved" [7]. In summary, the detailed mechanism of eruptive boiling remains unclear, possibly due to lack of proper flow visualization tools.

This investigation elucidates experimentally eruptive boiling heat transfer in the silicon-based microchannel which is with a width of 99.8 μm, a depth of 20.3 μm and hydraulic diameter of 33.7 μm. The microchannels were made of SOI wafer and prepared using bulk micromachining and anodic bonding processes. The two-phase flow

* Corresponding author.
E-mail address: cpan@ess.nthu.edu.tw (C. Pan).

0017-9310/$ - see front matter © 2008 Elsevier Ltd. All rights reserved.
doi:10.1016/j.ijheatmasstransfer.2008.02.033

Nomenclature

A	reference constant
c_1, c_2	reference constant
D_H	hydraulic diameter (μm)
G	mass flux (kg/m^2 s)
i_{lv}	latent heat of evaporation (J/kg)
k_l	thermal conductivity of liquid (W/m K)
P	pressure (kPa)
q''	wall heat flux (W/m^2)
q''_{ONB}	onset of nucleate boiling heat flux (W/m^2)
$r_{c,crit}$	critical cavity radius (m)
$r_{c,max}$	maximum cavity radius (m)
$r_{c,min}$	minimum cavity radius (m)
Re	Reynolds number
T	temperature (°C)
t_1, t_2	reference time (s)
T_∞	bulk liquid temperature (°C)
T_{sat}	saturation temperature (°C)
T_w	wall temperature (°C)
v_{lv}	the specific volume difference between vapor and liquid (m^3/kg)

Greek symbols

$\Delta T_{sat,ONB}$	onset of nucleate boiling wall superheat (°C)
σ	surface tension (N/m)
θ	contact angle (°)

patterns under boiling conditions were visualized using a high-speed video camera with a ultra high frame rate and analyzed with simultaneous measurement of temperatures at the heating surface, the inlet and outlet chambers, and the pressure drop from inlet to outlet chambers to explore the two-phase flow and boiling heat transfer phenomena in the microchannel.

2. Experimental details

2.1. Experimental setup

Fig. 1a schematically depicts the experimental setup, consisting of a high-performance liquid chromatography (HPLC, Dionex P680) pump, the test section with a rectangular microchannel, a heating module and a flow visualization system. The test section was prepared by a combination of silicon dry etching (Deep Reactive Ion Etching) with photolithography and anodic bonding process of Pyrex glass for flow visualization. Fig. 1b depicts a top view of the test section. The test section is a silicon strip, 10 mm by 40 mm, with a microchannel, and inlet and outlet chambers etched in the central part. The width and depth of the microchannel are 99.8 μm and 20.3 μm, respectively, resulting in a hydraulic diameter of 33.7 μm and a depth-to-width ratio of 0.203. The inlet and outlet chambers were etched with dimensions of 2 mm × 3 mm. A ruler with minor divisions of 30 μm was also etched on the top surface, enabling the identification of the location and the size of each bubble. A scanning electron microscope (SEM) was utilized to verify the dimensions of the prepared microchannels, as displayed in Fig. 1c. The surface roughness of the channel wall, including the bottom and side walls, possibly with nano-dusts, was examined by an atomic force microcopy outside the clean room after experiment, as presented in Fig. 2, and the maximum heights of the bottom and side walls for the region scanned are 0.942 μm and 0.874 μm, respectively. It is believed that the nano-dusts were introduced into the channel from air after the Pyrex glass was removed. Since the channel is relatively shallow, the surface roughness of the side wall is approximately the same as that of the bottom one.

The test section with the silicon-based microchannel adhered with silver composition to the top of the heating module, which is a copper (C1100, Cu $\geqq$ 99.90, $P \leqq$ 0.0004) block that was heated by a heating element with controllable power. Five T-type thermocouples were embedded in the copper block. Three thermocouples were located 2 mm under the heating surface along the channel. The temperatures at the three locations were within 0.8 °C even under high heat flux conditions. Accordingly, the temperature measured by the central thermocouple was used to extrapolate the temperature of the channel wall, with reference to the measured contact resistance [8].

The test section and the heating module were covered with ceramic fiber to minimize heat loss, while the top of the test section was used for flow visualization. The heat loss caused by natural convection and thermal radiation from the Pyrex surface, together with the heat losses by conduction to the inlet and outlet chambers were estimated to determine the channel heating power under boiling conditions [8].

The temperatures at the inlet and outlet chambers were measured using T-type thermocouples. The absolute pressure at the joint in front of the inlet chamber and the differential pressure between the inlet and outlet joints, as presented in Fig. 1a, were measured using an absolute pressure transducer (Huba Control UK/model: 691) and a differential pressure transducer (Huba Control UK/model: 692), respectively. The range of the measurements was from 0 to 1000 kPa with corresponding output signals from 4 to 20 mA. The uncertainty and response time of the transducers are ±0.5% off span and 5 ms, respectively. The output of the thermocouples and the pressure transducers was recorded by a data acquisition system (YOKOKAWA MX100). The pressure at the outlet fixture is very close to atmospheric pressure. The minor pressure losses in the present microchannel system are insignificant.

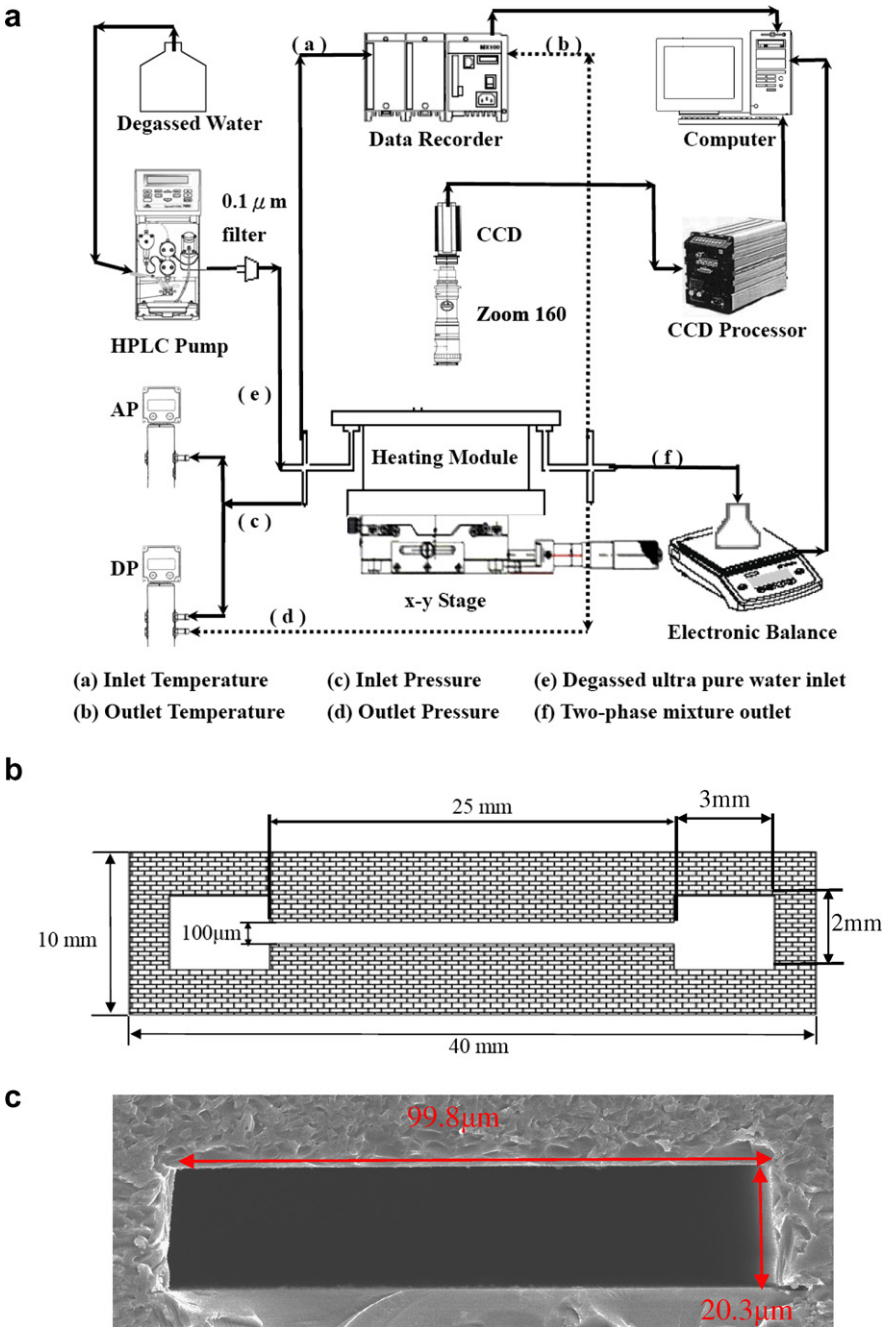

Fig. 1. (a) Schematic of the experimental setup; (b) top view of the microchannel (length show not to scale) and (c) the geometry of the microchannel with $D_H = 33.7$ μm.

For instance, for a mass flux (G) of 625 kg/m^2 s, the total pressure drop for the single-phase flow of liquid water through the test channel and inlet/outlet chambers is 403 kPa at room temperature, while the secondary losses associated with the sudden contraction at the inlet and the sudden expansion at outlet are estimated to be 0.20 kPa and 0.10 kPa, respectively.

The flow of degassed ultra pure water, with an electric resistance of 18 MΩ/cm, in the microchannel, was driven by the HPLC pump, described above. At flow rates from 1 μl/min to 10 ml/min and operating pressures of up to 50 MPa, the pump is suitable for the present investigation. A MILLIPORE membrane filter with a net size of 0.1 μm was installed at the exit of the HPLC pump to filter micro-size particles. Tests were conducted at heat fluxes (q'') of 0.15–372 kW/m^2 and mass fluxes of 209–625 kg/m^2 s, corresponding to Reynolds numbers of 7.72–23.2.

The flow visualization system includes a high-speed digital camera (PHOTRON FASTCAM-Ultima APX CMOS camera), a monitor and a personal computer. A microlens (OPTEM Zoom 160) was mounted on the CCD to observe the two-phase flow pattern in the microchannel. The micro-

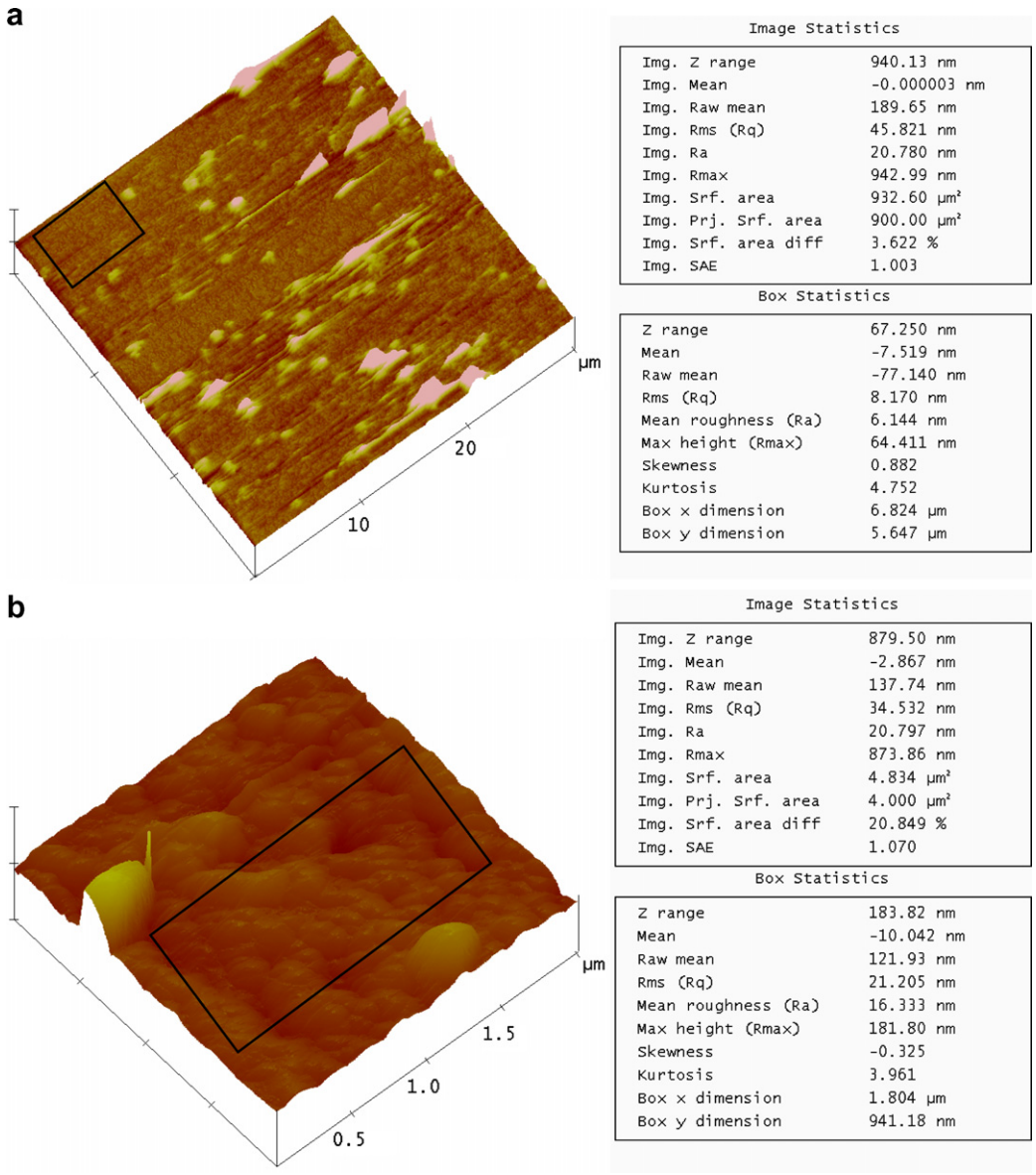

Fig. 2. Surface roughnesses examined using an atomic force microscope: (a) bottom wall and (b) side wall.

lens provides a 16:1 zoom ratio and an overall magnification range of 680–1. The maximum available frame rate of the camera was 120,000 frames/s and the maximum shutter speed was 1/120,000 s^{-1}. The frame rate was normally set at 15,000 frames/s at a 1024×128 resolution and the area of the recorded images was 1 mm × 125 μm. In cases with very rapid bubble growth, the frame rate was set at 50,000 frames/s at a 256×64 resolution and the area of the recorded images was 250 μm × 62.5 μm. A test module was installed in an x–y–z mechanism to hold the lens and to position accurately the test plane (x–y plane) and to ensure accurate focusing (z-direction).

The measurement uncertainty for volume flow rate in the microchannels after calibration was estimated to be ±0.27%. The uncertainties in temperature measurements were ±0.2 °C for the T-type thermocouples. The uncertainty of wall heat flux under flow boiling wall heat flux is ±1.49% to ±39.5% with an average value of ±9.04%. The uncertainty generally decreases with increasing heat flux and/or mass flux.

2.2. Fabrication of test section

In order to eliminate the loading effect of a deep reactive ion etching (DRIE) processes, the test section was made of P-type ⟨1 0 0⟩ orientation SOI (Silicon on Insulator) wafer and was etched with microchannels on its handle layer surface. In the present study, SOI wafer consists of three basic layers (from bottom to top): (1) handle layer: 525 ± 25 μm bare wafer (100, P-type, polishing); (2) box layer: 0.5 μm SiO_2 (thermooxide); (3) device layer: 20 μm silicon (100, P-type, polishing). The test section was a 10-mm wide silicon stripe and was etched with microchannels on its device layer surface. The fabrication process of the microchannels,

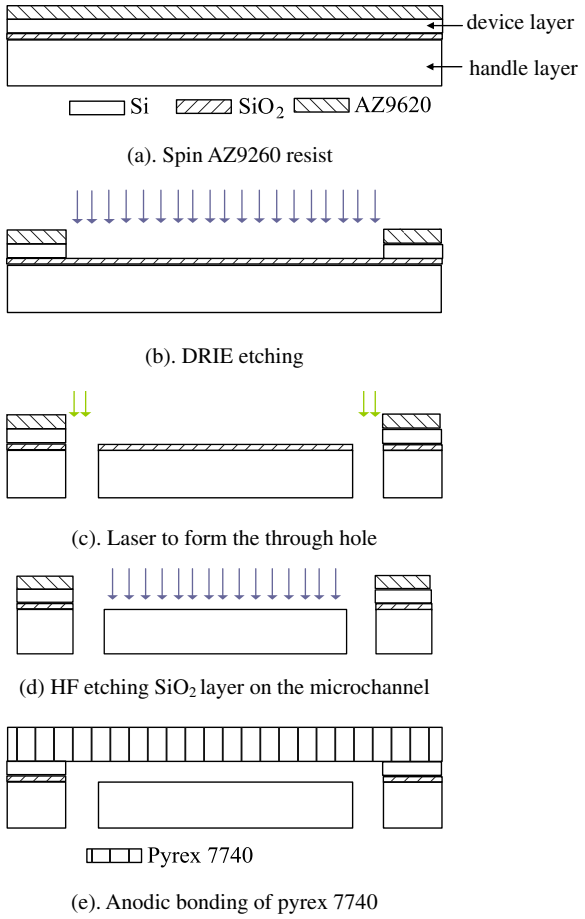

Fig. 3. Schematic of fabrication process.

shown in Fig. 3, employed silicon DRIE etching with photolithography and anodic bonding process. The process started from the bulk etching passivation of 5 μm AZ9620 using spin (Fig. 3a). The DRIE, as shown in Fig. 3b, was to form the microchannel. The laser cutting was performed to make the through holes (Fig. 3c) as the inlet and outlet sumps of microchannel. HF liquid was then applied to etch the SiO_2 layer at the bottom wall of the microchannel (Fig. 3d). To enable flow visualization, the top surface was covered with Pyrex 7740 glass through anodic bonding (Fig. 3e).

3. Results and discussion

Fig. 4a and b shows two series of images of eruptive boiling in the microchannel from the side and bottom walls, respectively. As indicated earlier, the aspect ratio of the channel is approximately 0.2, revealing that the channel is shallower than it is wide. The frame rate in this case was as high as 24,000 frames/s. Fig. 4a demonstrates that, at a particular time t_1, a microbubble nucleates 330 μm upstream of a slug bubble. 1/24,000 s later, the bubble deforms downstream due to the drag of liquid flow. The deformation increases and at 3/24,000 s (0.125 ms) later, the deformed bubble merges with the slug bubble downstream, which tail end is approximately 330 μm from the nucleation site. Such bubble nucleation and merging with the slug bubble is completed within 0.12 ms, as confirmed at higher frame rate of 50,000 frames/s. The bubble then departed from the nucleation site at about 6/24,000 s after its nucleation. At 18/24,000 s the tail end of the slug bubble returns to its original location and another bubble nucleates from the same site. Thus, the bubble frequency for this particular period is 1333. Sampling frames 343 of the 20 bubble nucleations (24,000 frames/s) indicates a bubble frequency of 1399 Hz, as stated in Table 1. Since the nucleating bubble merges with the slug bubble within 0.12 ms, if this phenomenon is observed using a frame rate that is much smaller than 8000 frames/s, as show in Fig. 5, then it will appear as an oscillation of the tail interface of the slug bubble. Flow visualization confirms that eruptive boiling in the present study is nucleate boiling with ultra rapidly growing bubbles. The slug bubble downstream seems to have no effects on bubble nucleation upstream.

Fig. 4b demonstrates that, at a particular time t_2, a microbubble nucleates from the bottom wall and such bubble nucleation and departure from the active site is completed within 0.208 ms. Interestingly, there is no slug bubble downstream within the visualization window. It is at 184/24,000 s that another bubble nucleates from the same site. For this particular case, the bubble growth rate at the beginning is estimated to be about 0.28 m/s based on a series of images. The bubble eventually evolves to a slug bubble, which length grows exponentially [12]. The bubble growth are estimated to be 0.30 m/s and 0.04 m/s for $G = 625\ \mathrm{kg/m^2\,s}$ and $q'' = 218\ \mathrm{kW/m^2}$ and 372 kW/m^2, respectively. For the latter case, three bubbles are nucleating nearby downstream after the bubble under consideration is nucleated. The bubble grows exponentially for the case of $G = 625\ \mathrm{kg/m^2\,s}$ and $q'' = 153\ \mathrm{kW/m^2}$ with a coefficient in the exponent of about $3070\ \mathrm{s^{-1}}$. It should be noted, however, the bubble grows very rapidly for the eruptive boiling reported in this study and it is difficult to determine the bubble edge accurately. Indeed, the bubble growth rate cannot be determined meaningfully for the other five cases of this study.

Furthermore, eruptive boiling is also observed in a single shallow diverging microchannel with approximately the same channel depth and mean hydraulic diameter prepared by same processing steps as show in Fig. 6. The silicon microchannel that was employed by Zhang et al. was also prepared using DRIE, with the same order of magnitude of surface roughness. Indeed, they employed a cavity size of 0.1–0.4 μm in the 45 μm channel to make good predictions using Hsu's model [11].

Eruptive boiling occurred in all cases in this study. Table 1 summarizes the effect of mass flux and heat flux on the location of the onset of nucleate boiling (ONB), bubble frequency and critical cavity size, determined using Eq. (2). At a given flow rate, the ONB location moves upstream as the heat flux is increased, as in an ordinarily sized channel. The bubble frequency was determined from the sampling

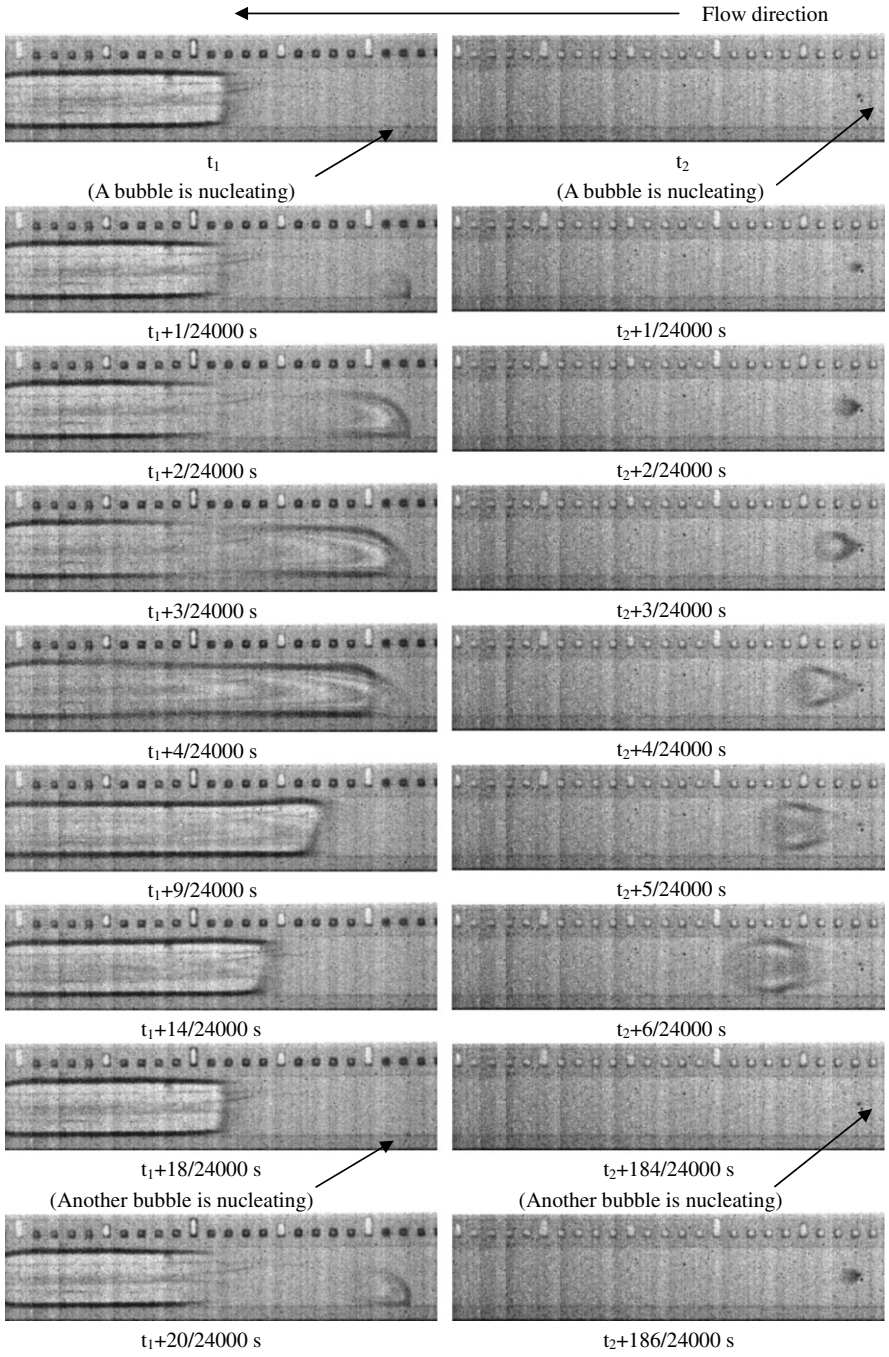

(a) Nucleation site at z = 24.54 mm from inlet

(b) Nucleation site at z = 14.16 mm from inlet

Fig. 4. Eruptive bubble nucleation in the microchannel: (a) from side wall, $G = 417\ \mathrm{kg/m^2\,s}$, $q'' = 14.9\ \mathrm{kW/m^2}$, $T_w = 119\ ^\circ\mathrm{C}$ and (b) from bottom wall, $G = 625\ \mathrm{kg/m^2\,s}$, $q'' = 218\ \mathrm{kW/m^2}$, $T_w = 137\ ^\circ\mathrm{C}$.

frames, yielding 11–20 nucleating bubbles for a particular frame rate employed. The bubble frequency ranges from 54.0 to 2000 Hz, and, in general, declines as the heat flux increases for a given flow rate. This may be explained by the fact that ONB moves to an upstream location and the local pressure increases as the heat flux increases. Eq. (1) yields heat flux (q''_{ONB}) and wall superheats ($\Delta T_{\mathrm{sat,ONB}}$) for the ONB from a smooth surface, given the channel walls in this work [9], if the maximum cavity size is smaller than the critical cavity size, which is given by Eq. (2) [10]:

$$q''_{\mathrm{ONB}} = \frac{k_l}{r_{\mathrm{c,max}}}\Delta T_{\mathrm{sat,ONB}} - \frac{2\sigma k_l T_{\mathrm{sat}} v_{\mathrm{lv}}}{i_{\mathrm{lv}} r^2_{\mathrm{c,max}}}, \tag{1}$$

$$r_{\mathrm{c,crit}} = \left(\frac{2\sigma T_{\mathrm{sat}} v_{\mathrm{lv}} k_l}{i_{\mathrm{lv}} q''_{\mathrm{ONB}}}\right)^{1/2}, \tag{2}$$

Table 1
Effect of heat flux and mass flux on ONB location, bubble frequency and critical cavity size

q'' (kW/m^2)	T_w (°C)	ONB location (distance from inlet, mm)/ estimated local pressure (kPa)	f (Hz)/No. of bubble nucleated (sampling frames/ recording rates)	$r_{c,crit}$ (μm)
G = 625 (kg/m^2 s)				
16.6	114	24.54/102	2000/20 (240/24,000)	29.2
84.2	116	24.48/103	1337/20 (359/24,000)	13.0
153	126	17.01/147	68.9/20 (2332/8000)	9.39
218	137	14.16/182	128/16 (2966/24,000)	7.45
286	145[b]	11.04[a]/244	277/20 (1735/24,000)	6.05
372	153[b]	5.34/361	80.4/11 (3285/24,000)	4.94
G = 417 (kg/m^2 s)				
14.9	119	24.54/138	1399/20 (343/24,000)	32.9
129	123	21.06[2]/190	792/20 (202/8000)	10.0
181	131	9.81/238	54.0/18 (2668/8000)	8.34

[a] Bubbles may be generated intermittently from the inlet chamber.
[b] Partial dryout.

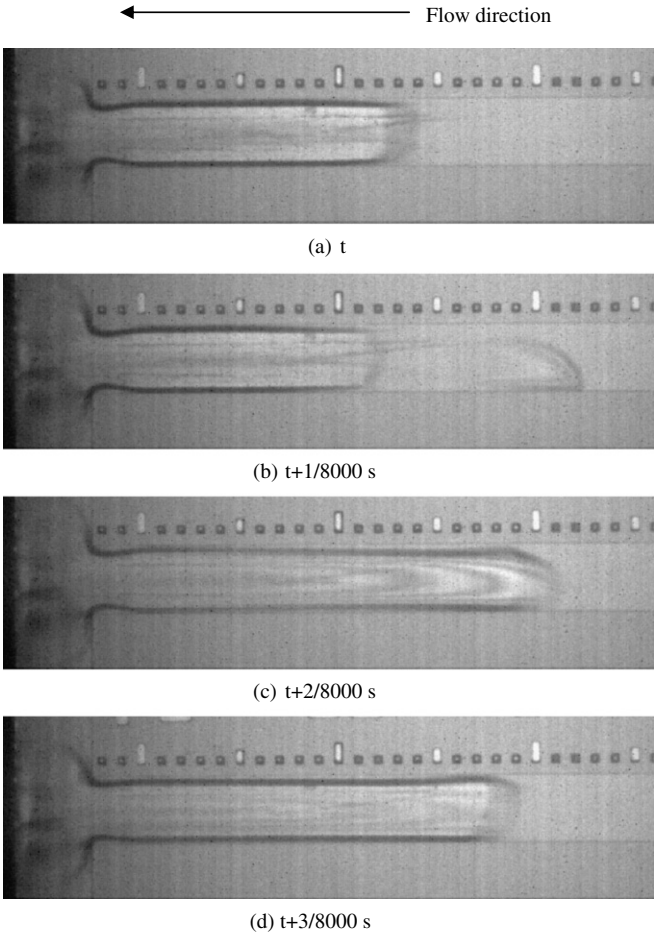

Fig. 5. The eruptive bubble nucleation shown in Fig. 4a as observed a frame rate of 8000 frames/s.

where k_l is the thermal conductivity of the liquid (water), σ is the surface tension, v_{lv} is the difference in specific volume between vapor and liquid, i_{lv} is the latent heat of evaporation, T_{sat} is the saturation temperature and $r_{c,max}$ is the maximum cavity size available on the surface. Indeed, in this investigation, the critical cavity size, $r_{c,crit}$ is from 4.94 μm to 32.9 μm, as shown in Table 1, and decreases with increasing heat flux. Clearly, all of the critical cavity sizes exceed the largest cavity that is available, and the onset of nucleate boiling is governed by Eq. (1).

Fig. 7 compares the data herein with predictions of Eq. (1) for various different values of $r_{c,max}$. With reference to the experimental data points in Fig. 7, the saturation temperature corresponds to the local pressure at each of the ONB locations. The local pressure is estimated by assuming a linear pressure distribution in the channel between the inlet and the outlet. As for the solid curves, which are evaluated using Eq. (1), the saturation temperature and the thermophysical properties correspond to the saturation state of the system pressure, which is the arithmetic mean of the inlet and outlet pressures. The system pressure may vary from case to case, and a mean system pressure of 205.6 kPa over all cases is employed. The figure demonstrates that most of the cavity sizes range from 0.6 to1.3 μm. This result is consistent with the maximum roughness of the bottom wall, 0.942 μm, and the side wall, 0.874 μm, as revealed above in Fig. 2a and b.

Eq. (1) suggests that, for a particular set of (q''_{ONB}, $\Delta T_{sat,ONB}$), $r_{c,max}$ has two distinct roots, given by

$$r_{c,max} = \frac{k_l \Delta T_{sat,ONB}}{2q''_{ONB}} \pm \frac{1}{2q''_{ONB}} \times \sqrt{k_l^2 \Delta T_{sat,ONB}^2 - 8q''_{ONB} \frac{\sigma k_l T_{sat} v_{lv}}{i_{lv}}}. \quad (3)$$

Fig. 8 plots the smaller root of $r_{c,max}$ against q''_{ONB} for all cases in this study. It is of the order of 10^{-6} μm and corresponds to the cavity size. Eq. (3) indicates that a double root of $r_{c,max}$ that equals as the critical cavity size, given by Eq. (2) exists when the $\Delta T_{sat,ONB}$ and q''_{ONB} are related by the following equation with a discriminant of zero. Notably, Eq. (4) is of the same form as the boiling nucleation criterion, assuming cavities of all sizes are present on the surface [9].

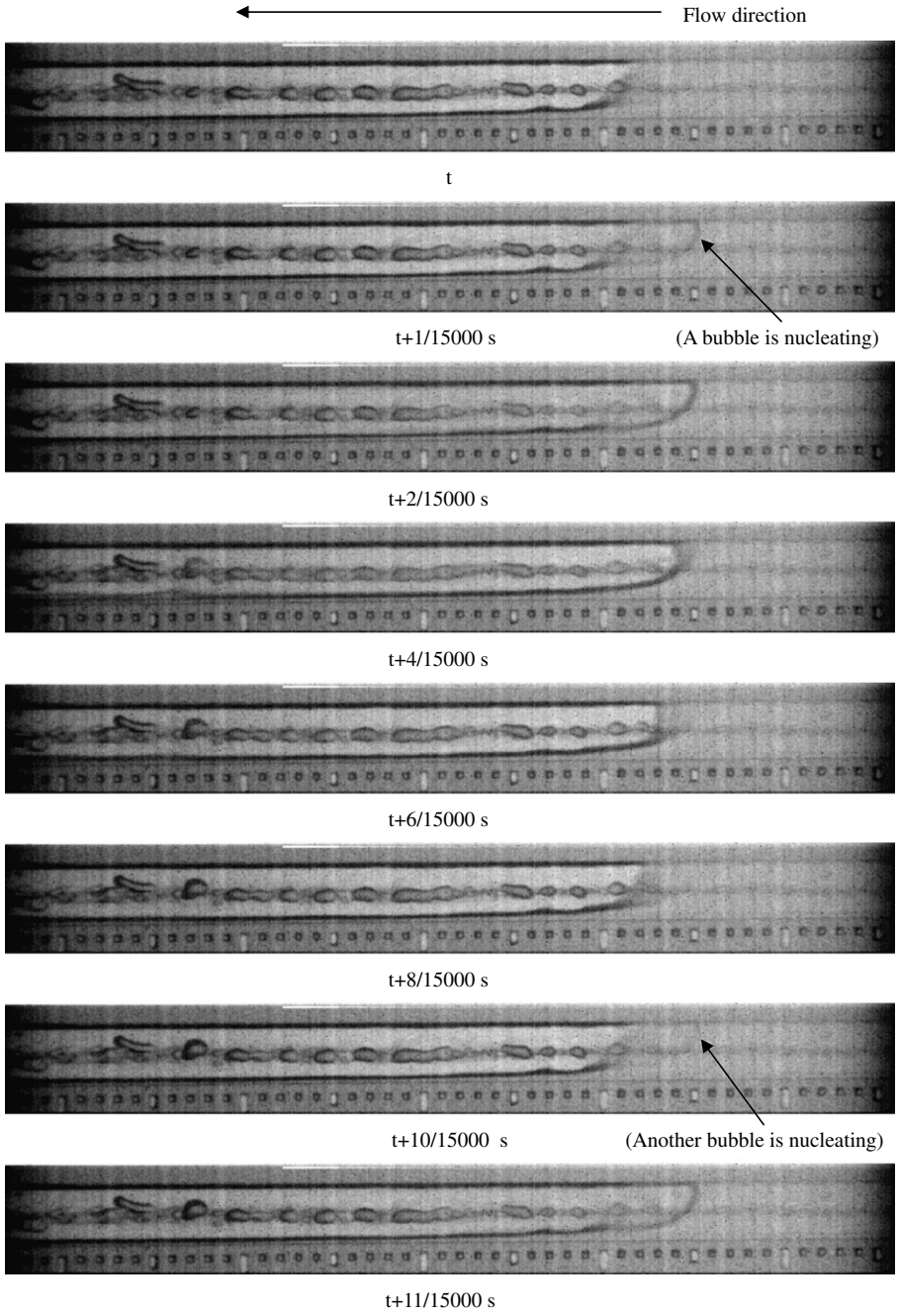

Fig. 6. Eruptive bubble nucleation in the diverging microchannel with a diverging angle of 0.183° and nucleation site at $z = 11.6$ mm from inlet ($G = 209$ kg/m^2 s based on the cross section area at the middle of the channel, $T_w = 147$ °C, $q'' = 226$ kW/m^2).

$$\Delta T^2_{sat,ONB} = q''_{ONB}\frac{8\sigma T_{sat} v_{lv}}{i_{lv} k_l}. \quad (4)$$

Hsu's model also predicts the ONB [11]. Indeed, Zhang et al. [3] used Hsu's model with one half of the channel hydraulic diameter as the thickness of the thermal boundary layer to predict the ONB in the sub-150 μm diameter microchannels, although they reported eruptive boiling in a sub-50 μm diameter channel "without a detectable bubble nucleation period". Fig. 8 also plots the minimum active cavity size ($r_{c,min}$) that is predicted by Hsu's model [11]:

$$r_{c,\min} = \frac{\delta}{2C_2}\frac{T_w - T_{sat}}{T_w - T_\infty}\left[1 - \sqrt{1 - \frac{4AC_2}{\delta}\frac{(T_w - T_\infty)}{(T_w - T_{sat})^2}}\right],$$
$$A = \frac{2\sigma}{C_1}\frac{T_{sat} v_{lv}}{i_{lv}}; \quad C_1 = \frac{1}{\sin\theta}; \quad C_2 = \frac{1+\cos\theta}{\sin\theta} \quad (5)$$

where δ is the thermal boundary layer thickness, θ is the contact angle, T_w is the wall temperature and T_∞ is the bulk liquid temperature. C_1 and C_2 in above equation are constants that are related to the contact angle for water

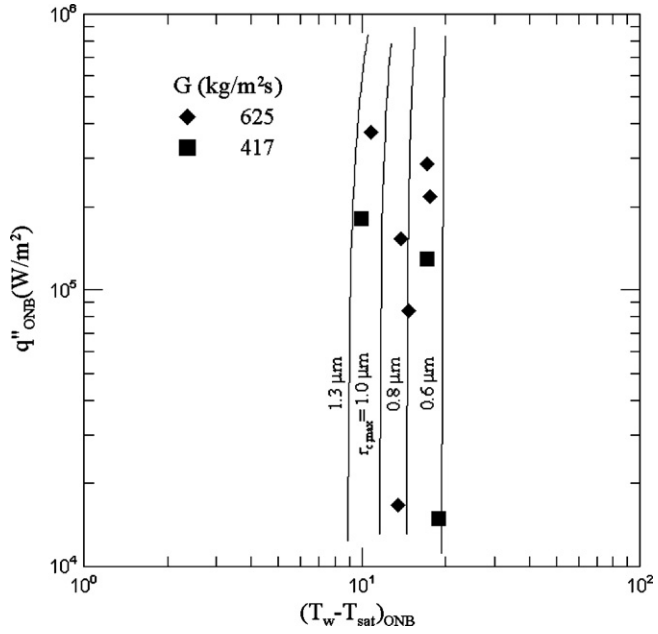

Fig. 7. Relationship between heat flux and wall superheat at the position of incipient boiling.

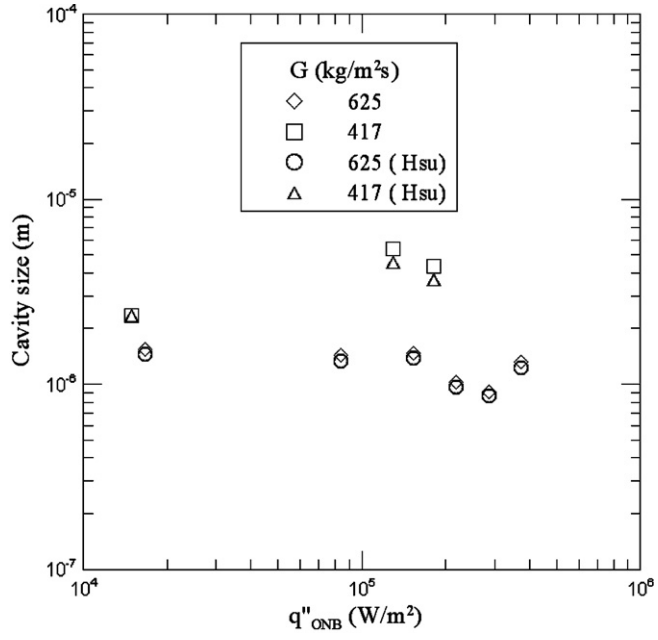

Fig. 8. Comparison between lower roots of $r_{c,max}$ and the $r_{c,min}$ predicted by Hsu's model.

on the silicon surface, which is approximately 70°, such that C_1 and C_2 are 1.06 and 1.43, respectively. The thickness of the thermal boundary layer is assumed to be half of the channel width. T_∞ is assumed to be equal to T_{sat} at the ONB site. Fig. 8 demonstrates good agreements between the lower root of $r_{c,max}$ given by Eq. (3) and the minimum cavity size that is predicted by Hsu's model.

4. Summary and conclusions

Eruptive boiling in a single shallow rectangular microchannel was investigated experimentally in the present work. The following conclusions may be draw from the results of the study:

1. Eruptive boiling is identified as a form of rapid bubble nucleation after which the bubble may merge with a slug bubble downstream in a short distance or evolve to a slug bubble.
2. Eruptive boiling may be predicted classically with nano-sized cavities that are consistent with the measured surface roughness.

Acknowledgements

The authors would like to thank the National Science Council of Taiwan, ROC, for financially supporting this research under Contract No. NSC-94-2212-E-007-056.

References

[1] M.J. Ellsworth, Chip power density and module cooling technology projections for the current decade, in: Proceedings of the International Society Conference on Thermal Phenomena, 2004, pp. 707–708.
[2] I. Mudawar, Assessment of high-heat-flux thermal management schemes, IEEE Trans. Compon. Pack. Technol. 24 (2001) 122–141.
[3] L. Zhang, E.N. Wang, K.E. Goodson, T.W. Kenny, Phase change phenomena in silicon microchannels, Int. J. Heat Mass Transfer 48 (2005) 1572–1582.
[4] D.W. Jeong, K.U. Koh, S.Y. Lee, Preliminary consideration to avoid eruptive flow boiling in microchannels, in: Proceedings of the First International Microchannel and Minichannel, USA, 2003, pp. 609–614.
[5] L. Jiang, J.M. Koo, S. Zeng, J.C. Mikkelsen, L. Zang, P. Zhou, J.G. Santiago, T.W. Kenny, K.E. Goodson, Two-phase microchannel heat sinks for an electrokinetic VLSI chip cooling system, in: Proceedings of Seventeenth IEEE SEMI-THERM Symposium, 2001, pp. 153–157.
[6] G. Hetsroni, A. Mosyak, E. Pogrebnyak, Z. Segal, Explosive boiling of water in parallel micro-channels, Int. J. Multiphase Flow 31 (2005) 371–392.
[7] S. Hardt, B. Schider, D. Tiemann, G. Kolb, V. Hessel, P. Stephan, Analysis of flow pattern emerging during evaporation in parallel microchannel, Int. J. Heat Mass Transfer 50 (2007) 226–239.
[8] P.C. Lee, F.G. Tseng, C. Pan, Bubble dynamics in microchannel. Part I: single microchannel, Int. J. Heat Mass Transfer 47 (2004) 5575–5589.
[9] R. Hino, T. Ueda, Studies on heat transfer and flow characteristics in subcooling flow boiling – Part 1. Boiling characteristics, Int. J. Multiphase Flow 11 (1985) 269–282.
[10] J.G. Collier, J.R. Thome, Convective Boiling and Condensation, third ed., Clarendon Press, Oxford, UK, 1994, p. 191.
[11] Y.Y. Hsu, On the size range of active nucleation cavities on a heating surface, ASME J. Heat Transfer 41 (1962) 207–216.
[12] P.C. Lee, C. Pan, Boiling heat transfer and two-phase flow in a single shallow microchannel with uniform or diverging cross-section, J. Micromech. Microeng. 18 (2008) 025005.